Kinetic Modeling of API Oxidation: 2. Imipramine Stress Testing

Haoyang Wu[a], Alon Grinberg Dana[a,b], Duminda S. Ranasinghe[a], Frank C. Pickard IV[c], Geoffrey P. F. Wood[c], Todd Zelesky[c], Gregory W. Sluggett[c], Jason Mustakis[c], William H. Green[a,*]

[a] *Department of Chemical Engineering, Massachusetts Institute of Technology, Cambridge, MA 02139, United States*
[b] *Wolfson Department of Chemical Engineering, Technion – Israel Institute of Technology, Haifa 3200003, Israel*
[c] *Pfizer Global Research & Development, Groton Laboratories, Eastern Point Road, Groton, CT 06340, United States*

Supporting Information

Model chemistry selection and calculated reaction rate coefficients

To address the challenges mentioned in section 3.2.2, we adopted several methods to reduce computational costs and improve accuracy in *ab initio* energy calculations. We partitioned the large-size imipramine molecule into easier-to-compute smaller fragments during *ab initio* calculations (Figure S1). We used a multi-structure approach to account for conformational effects to improve calculated rate coefficients and avoided the expensive hindered rotor scans. Moreover, we adopted the composite method approach that aims to achieve high accuracy by combining *ab initio* calculations with carefully-chosen level of theories. Geometry optimizations and frequency calculations were conducted using the ωB97X-D functional, [1] which benchmark studies have shown to be very effective at modeling chemical reactions and transition state geometries. [2] DLPNO-CCSD(T) was chosen for the single-point energy calculation method because recent literature has indicated that the accuracy of DLPNO-CCSD(T) is on par with the well-recognized but expensive CBS-QB3 method, and that DLPNO-CCSD(T) offers exceptional overall value relative to its DFT-like computational cost. [3, 4, 5, 6, 7, 8]

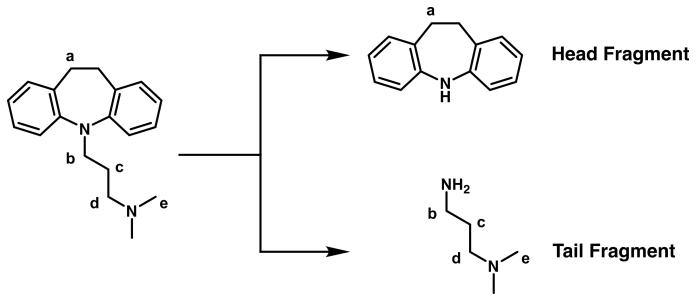

Figure S1: Chemical structures of imipramine fragments served as surrogates in *ab initio* reaction rate coefficients calculations. Reaction rate coefficients between attacking radicals such as hydroperoxymethanol radical ($OHCH_2OO\cdot$) and reactive sites on imipramine molecule (labeled with letters) are estimated using calculation results from corresponding sites on the fragments.

*Corresponding author
Email address: whgreen@mit.edu (William H. Green)

Table S1: Calculated reaction rate coefficients using DLPNO-CCSD(T)/def2-TZVP/def2-TZVP//COSMO-RS//ωB97X-D/def2-TZVP model chemistry and the above mentioned fragment approach for initial hydrogen abstraction reaction between hydroperoxymethanol radical ($OHCH_2OO\cdot$) and five reactive sites on imipramine molecule (labeled with letters above).

Reaction Site	A ($m^3\ mol^{-1}\ s^{-1}$)	Ea ($kJ\ mol^{-1}$)
a	86	23
b	8	28
c	179	59
d	9416	44
e	134	27

Transition state conformer geometries

Transition state conformer geometries for reactions presented in Table S1 are obtained using the ACS software. Coordinates of the conformers are included in the "transition_state_conformers.txt" file.

The chemical kinetic model used in this work

Reaction rate coefficients and chemical species thermodynamics for the imipramine oxidative degradation model presented in this work are included in the "imipramine_kinetic_model.yml" file. This file can be read using the RMS software to simulate the dynamics of the modeled system in a batch reactor.

Predicted concentration profiles of key reactive species and intermediates at pH 6.2 and pH 10.7 are included in the attached excel files. Selected results at pH 10.7 are shown in Figure S2.

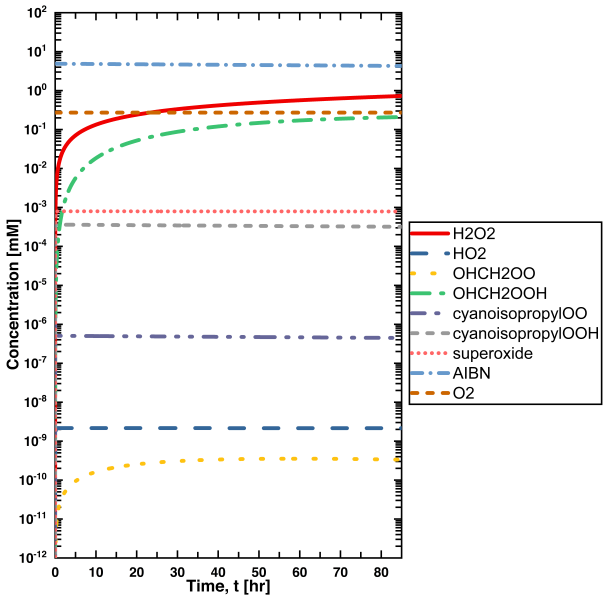

Figure S2: Predicted concentration profiles of key reactive species and intermediates in the imipramine degradation model at pH 10.7. The concentration profile data at pH 6.2 can be found in the attached excel files.

Degradation of imipramine under acidic conditions

This section presents the experimental results and model predictions for the degradation of imipramine under acidic conditions. To facilitate comparison, we have included again some results from the degradation of imipramine under basic conditions that have been discussed in detail in the main manuscript.

Degradation product yields were calculated on a molar concentration basis relative to the amount of imipramine consumed at 72 hours (Table S2). Imipramine consumed was 13.9% and 3.0% of initial concentration in the pH 6.2 and pH 10.7 conditions, respectively.

Table S2: Product yields for imipramine AIBN stress tests calculated on a molar concentration basis relative to the amount of imipramine consumed at 72 hours.

pH	**p2**	**p3**	**p4**	**p5**
6.2	27.8%	13.4%	1.0%	36.3%
10.7	44.7%	11.5%	1.5%	6.9%

The effective relative product distribution is summarized in Figure S3. Product **p2** was the major peroxyl radical derived degradation product for both protonated (pH 6.2) and neutral (pH 10.7) imipramine with 27.8% and 44.7% yield observed, respectively. The proportion of peroxyl radical oxidation at site **b** is reflected by the yield of **p2**, while the contribution of peroxyl radical oxidation at site **e** is the sum of **p3** and **p4** product yields. The pH had a minor impact on the peroxy radical derived reaction pathways, as the relative amount of **p2** was favored for both imipramine charge state conditions. The relative yield of N-oxide **p5** was higher at pH 6.2 than at pH 10.7 which may be consistent with decreased hydroperoxide stability under basic conditions. Mass balance of 97.0% and 98.9% was achieved for the pH 6.2 and pH 10.7 conditions, respectively, confirming that the UPLC method is suitably stability-indicating.

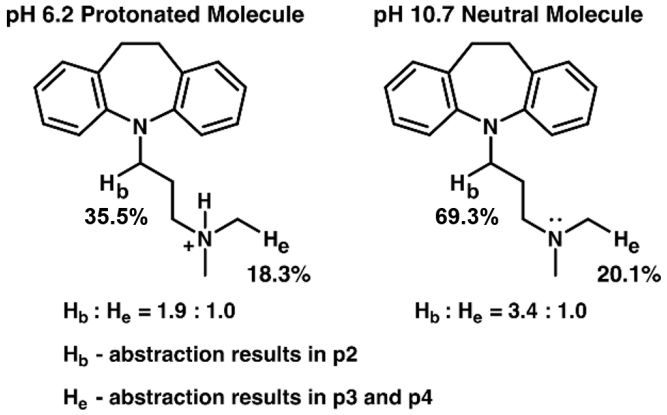

Figure S3: Effective relative product distribution of peroxy radical derived imipramine degradation products.

At pH 6, Zeneth predicted 5, 25 and 29 degradation products with likelihood scores of $\geq$ 800 (very likely), 600-799 (likely) and 400-599 (equivocal), respectively.

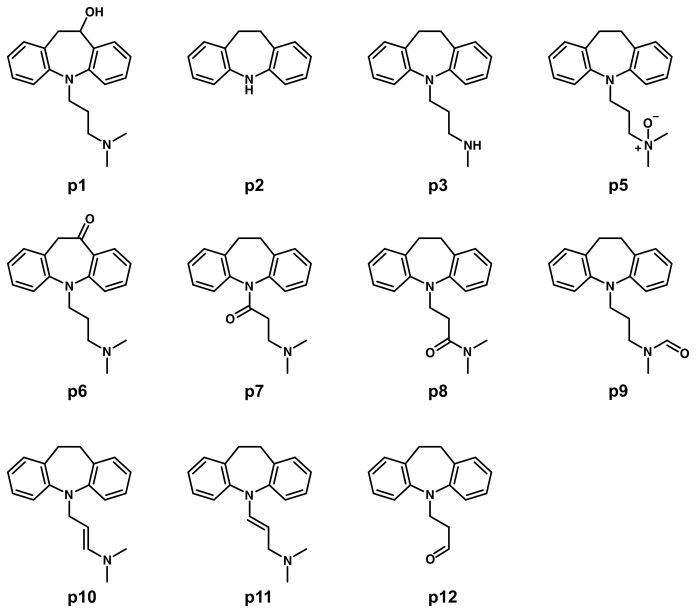

Figure S4: Pharmaceutically relevant one-step degradation products of imipramine due to free-radical oxidation at pH 6 as predicted by Zeneth. p1 and p6 had likelihood scores $\geq$ 800 (very likely); p2, p5, p7 and p11 had likelihood scores 600-799 (likely); p8, p10, and p12 had likelihood scores 400-599 (equivocal); p3 and p9 were not predicted (unlikely).

At pH 6, **p1**, **p2**, and **p3** are predicted to be the top three primary degradation products of imipramine.

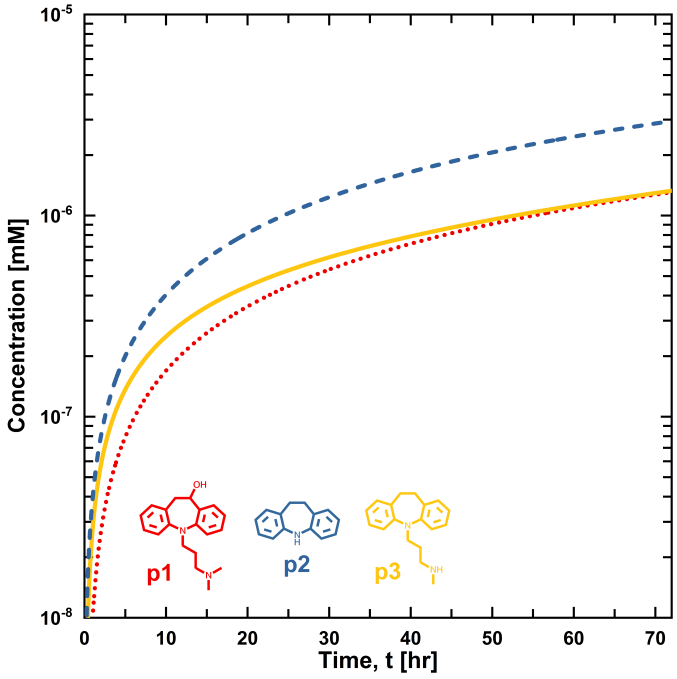

Figure S5: Predicted distribution of top three imipramine degradation products at pH 6 from *in silico* simulation.

Analytical LC

Table S3: Analytical LC Condition

Sample Description	**Column**	**Column Temp** **Flow rate** **Run time** **Detection λ**	**Mobile phase A/B**	**Gradient**
Imipramine HCl exposed to azoalkane stress conditions	Acquity HSS T3 C18 (100 mm x 2.1 mm i.d., 1.8 μm)	40°C 0.32 mL/min 18 min 211 nm	0.05% trifluoroacetic acid in water/CH_3CN	1-0.5 min: 15% B 0.5-10 min: linear increase 15-50% B 10-16 min: step gradient 50-95% B 16-16.1 min: step gradient 95-15% B 16.1-18.0 min: re-equilibration 15% B

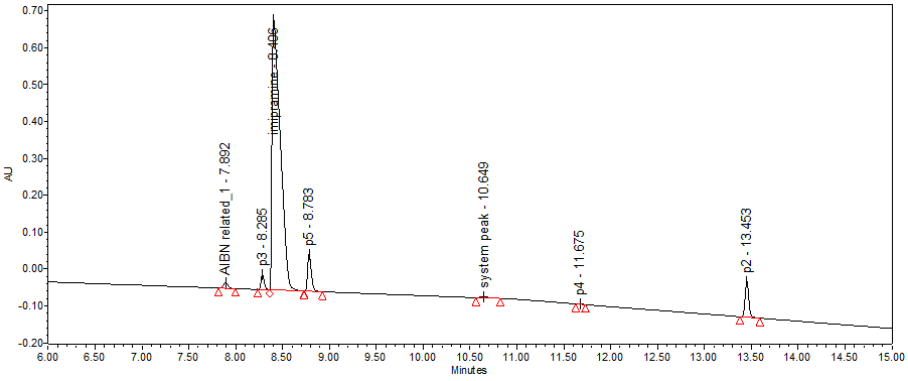

Figure S6: Expanded scale chromatogram of pH 6.2 imipramine HCl AIBN radical-initiated reaction

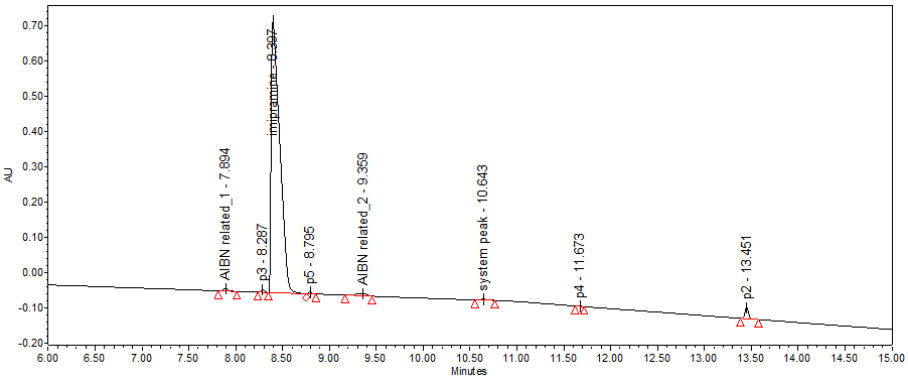

Figure S7: Expanded scale chromatogram of pH 10.7 imipramine HCl AIBN radical-initiated reaction

Product p2 and p3 Relative Response Factor (RRF) Determination Studies

Quantitative ^{1}H NMR (qNMR) standards and samples were prepared as follows. 1,3,5-trimethyoxybenzene was used as a certified reference standard with a potency factor of 99.96%. Samples were prepared in duplicate. 15-20 mg of **p2** and 8-10 mg 1,3,5-trimethyoxybenzene were dissolved in approximately 1 mL of

DMSO-d_6. Similarly, 15-20 mg of **p3** HCl and 8-10 mg 1,3,5-trimethyoxybenzene were dissolved in approximately 1 mL of DMSO-d_6. Samples were transferred to a 5 mm NMR tube. A Bruker Avance III NanoBay 400 MHz NMR was used for analysis. See Figure S8 - S11 for resultant ^{1}H NMR spectra. The potency factors for **p2** and **p3** were determined to be 98.5% and 86.8%, respectively. UPLC samples were prepared as follows. Duplicate imipramine HCl standards were prepared. 16-17 mg of imipramine HCl were transferred to a 25 mL volumetric flask and dissolved in 50/50 (v/v) water/acetonitrile diluent.

Approximately 6 mg of **p2** and 16 mg of **p3** were transferred separate 25 mL volumetric flasks and dissolved in 50/50 (v/v) water/acetonitrile diluent. A serial dilution of 1 mL to 25 mL was performed for each for UPLC injection. UPLC analysis was performed using Table S3 method. qNMR determined potency factors and UPLC determined imipramine HCl standard and sample response factors were used to calculate a UPLC relative response of 1.88 and 1.05 for **p2** and **p3** respectively.

Quantitative Nuclear Magnetic Resonance (qNMR) Experimental

All 1D data were collected at 298 K using a Bruker BioSpin 5mm BBFO probe on an AVANCE III NMR spectrometer (Bruker-BioSpin, Billerica, Massachusetts) operating at 400 MHz. For proton qNMR experiments, the relaxation delay was set to 30 seconds and the read pulse was set to 30° to ensure that signals have fully relaxed between pulses. The 1D proton spectra were referenced using residual solvent signal, set to 2.51 ppm.

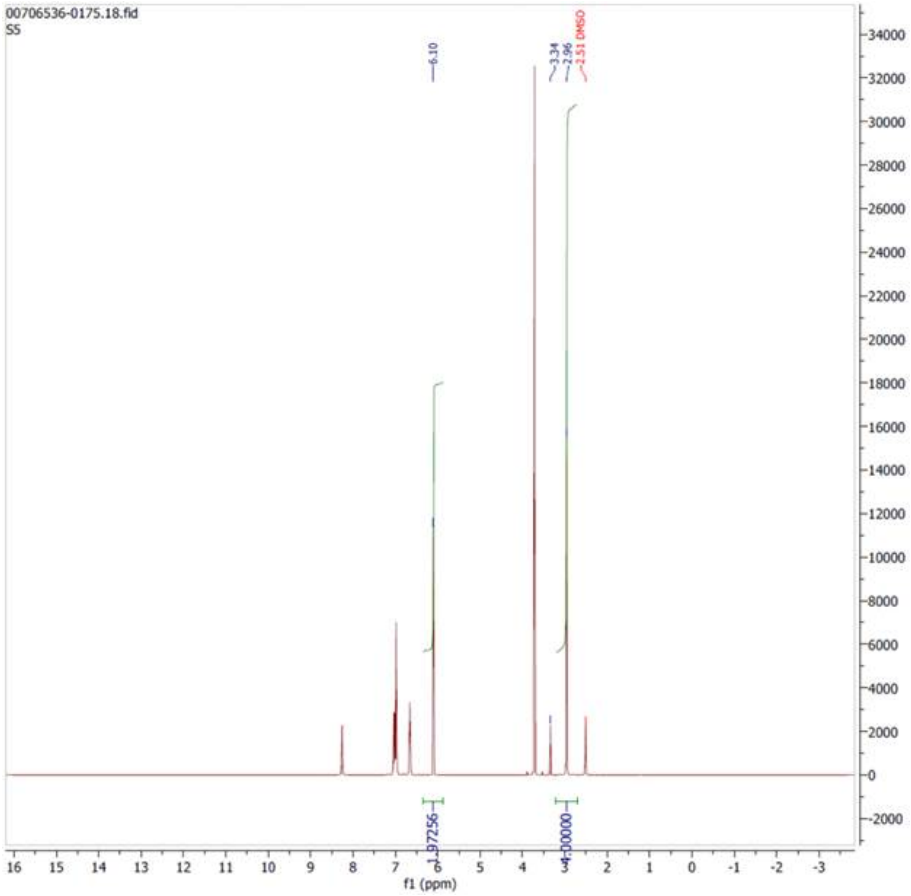

Figure S8: ^{1}H NMR spectra for 10,11-dihydro-5H-dibenzo[b,f]azepine **(p2)** qNMR study; sample 1

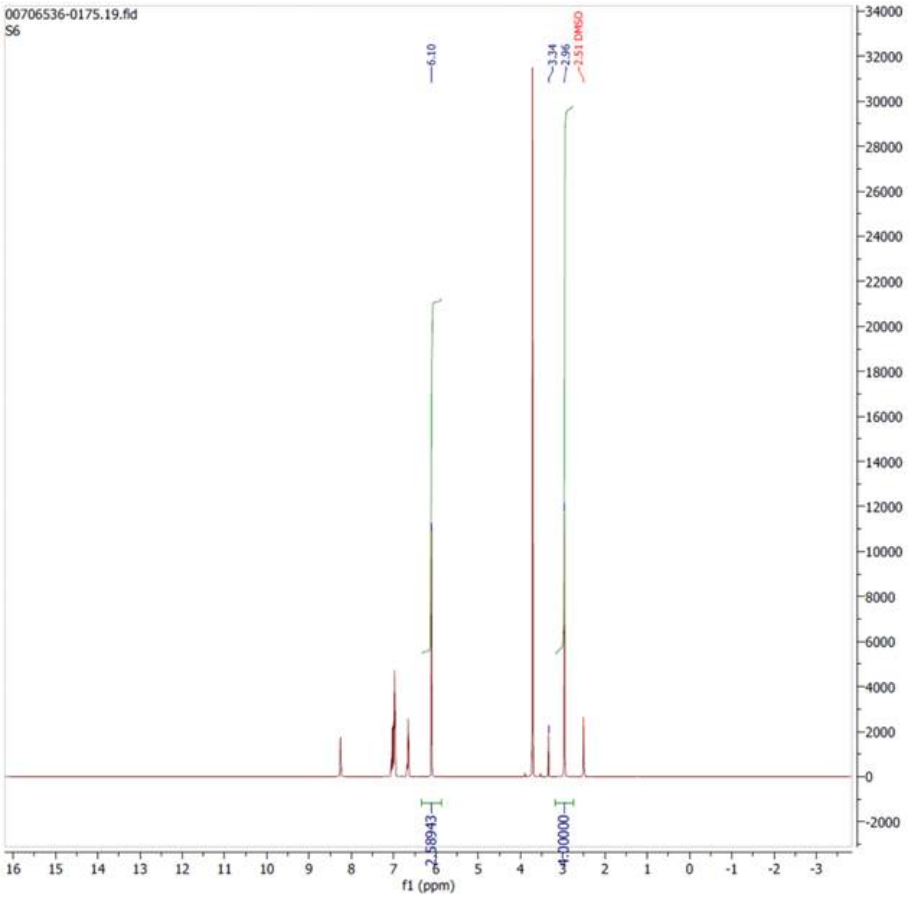

Figure S9: ^{1}H NMR spectra for 10,11-dihydro-5H-dibenzo[b,f]azepine **(p2)** qNMR study; sample 2

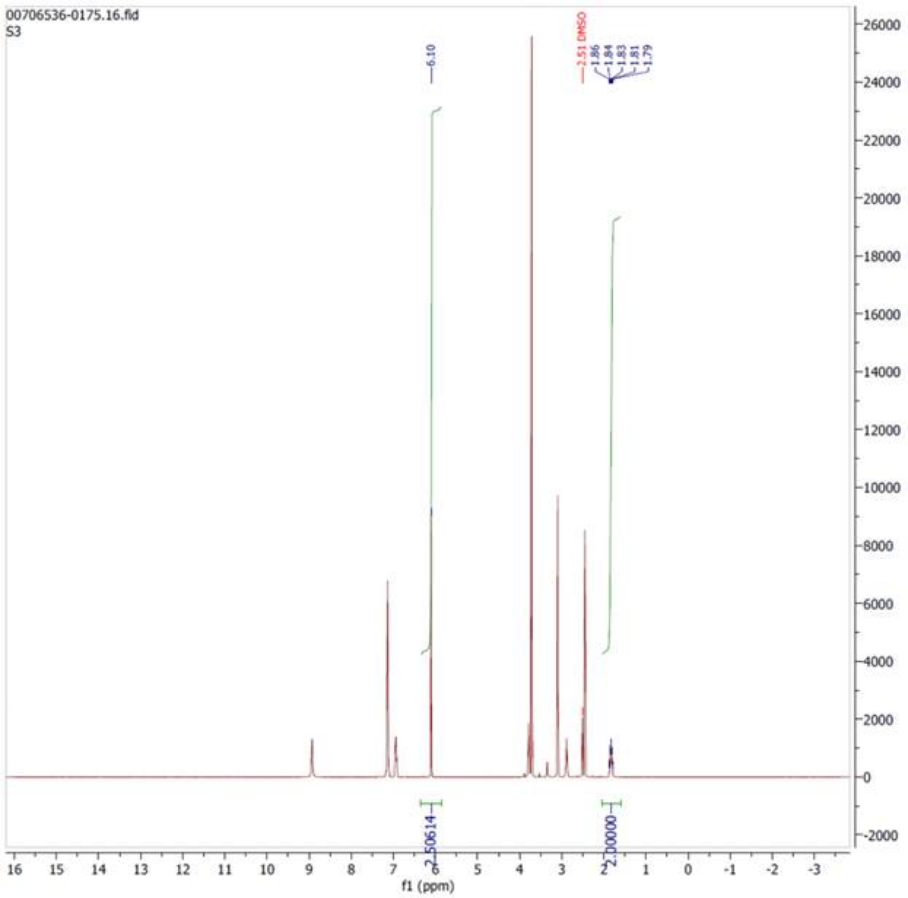

Figure S10: ^{1}H NMR spectra for 3-(10,11-dihydro-5H-dibenzo[b,f]azepin-5-yl)-N-methylpropan-1-amine **(p3)** HCl qNMR study; sample 1

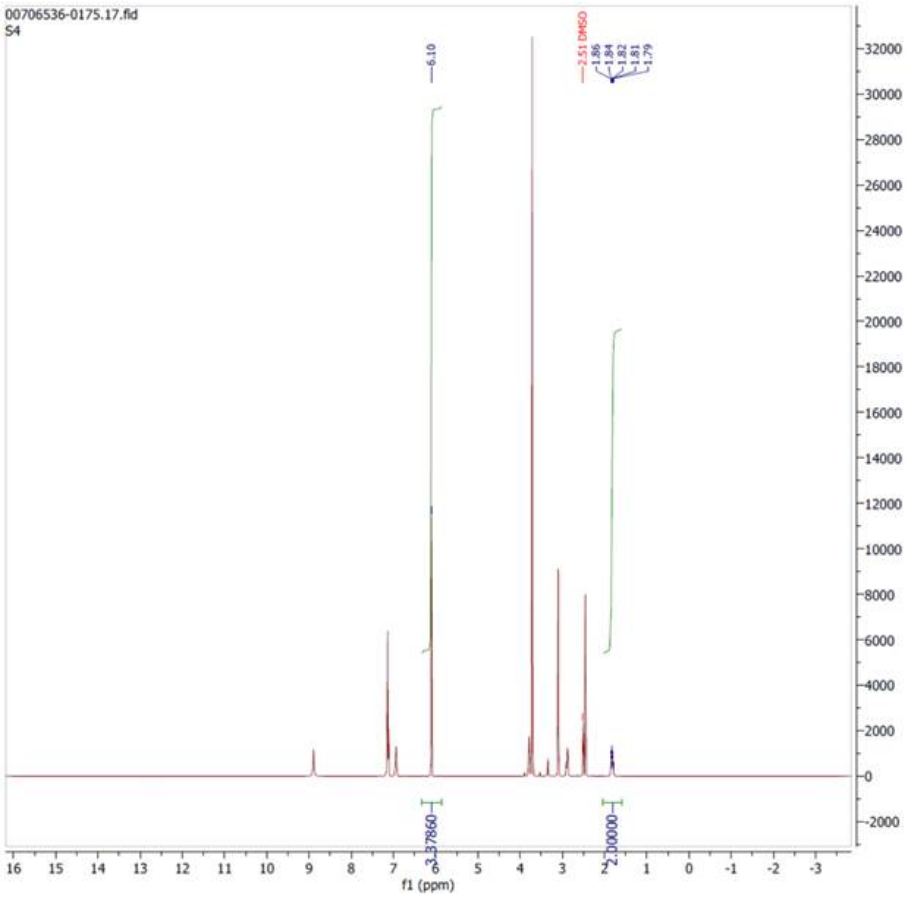

Figure S11: ^{1}H NMR spectra for 3-(10,11-dihydro-5H-dibenzo[b,f]azepin-5-yl)-N-methylpropan-1-amine **(p3)** HCl qNMR study; sample 2

Preparation of N-oxide (p5) for Structure Confirmation

Imipramine HCl (0.059 g, 0.186 mmol) was dissolved in 13.5 mL of water in a 20 mL glass scintillation vial. AIBN (0.098 g, 0.597 mmol) was dissolved in 16.6 mL of methanol in a separate 20 mL glass scintillation vial. Imipramine and AIBN solutions were combined and mixed well. ∼10 mL aliquots were transferred into three 20 mL glass scintillation vials. The three glass scintillation vials were placed into a general purpose Parr vessel and placed into a 60°C oven for 23 hours. Solutions were then combined. Methanol was removed via rotary evaporator. Approximately 25 mL water were added with solids filtered using a 0.45 μm syringe nylon membrane filter. The filtrate were passed through a conditioned and equilibrated Oasis HLB 20 cc (1 g) LP extraction cartridge at a rate of ∼2 drops/second, followed by a water wash and elution of crude reaction products with acetonitrile. Acetonitrile was removed via rotary evaporator and the resultant solids were reconstituted in ∼1.5 mL of methanol for SFC injection. Isolation of N-oxide (**p5**) was accomplished using method in Table S4.

Table S4: Preparative SFC Conditions

Sample Description	**Column**	**Column temperature** **Flow rate** **Run time** **Detection wavelength**	**Gradient**
Preparation of N-oxide (**p5**) for Structure Confirmation	Princeton PYR column, 2-ethylpyridine, 250 mm x 10 mm i.d., 5 μm	40°C 10 mL/min 7.2 min 211 nm	0-5.5 min: 10-43% MeOH 5.5-5.7 min: 43% MeOH 5.7-7.2 min: 10% MeOH

Mass Spectrometry Experimental

High-resolution and tandem mass spectrometric experiments for structure characterization were carried out in the positive ion mode using an Orbitrap Fusion Lumos mass spectrometer (Thermo Electron North America LLC) coupled with a heated electrospray ionization source (HESI). A spray voltage of 3.5 kV, sheath gas flow rate of 50 (in arbitrary units), and capillary temperature of 300°C were used. High-resolution data were acquired using a resolving power of 60,000 in full scan mode and 15,000 in the MS/MS scan mode. Tandem MS experiments were performed using higher-energy collision-induced dissociation (HCD) mode with structure-dependent normalized collision energy setting of 40 (in arbitrary units).

Mass Spectrometry Results for p4

High resolution accurate mass measurements of **p4** showed the molecular ion [M+H]+ at m/z value of 306.1965 that correlates to a protonated empirical formula of $C_{20}H_{24}N_3$+ with a deviation of 0.2 ppm from the theoretical mass. The MS^2 of m/z 306 gave a major fragment ion at m/z 111 resulting from the loss of the iminodibenzyl (**p2**) moiety. The MS^2 of m/z 306 yielded additional fragment ions m/z 195 (loss of 2-(methyl (propyl) amino) acetonitrile), m/z 83 (loss of 5-(ethyl) iminodibenyzl), m/z 208 (loss of 2-(ethyl(methyl)amino)acetonitrile), and m/z 234 (loss of (methylamino)acetonitrile).

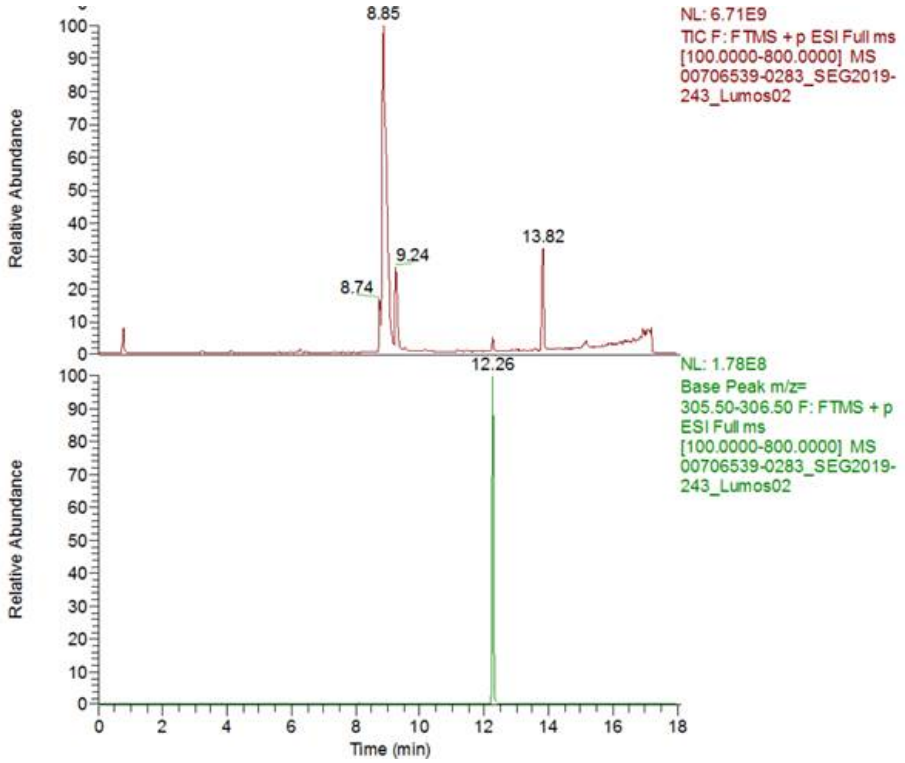

Figure S12: TIC and XIC (m/z 306) for pH 6.2 AIBN stressed imipramine day 3 reaction sample

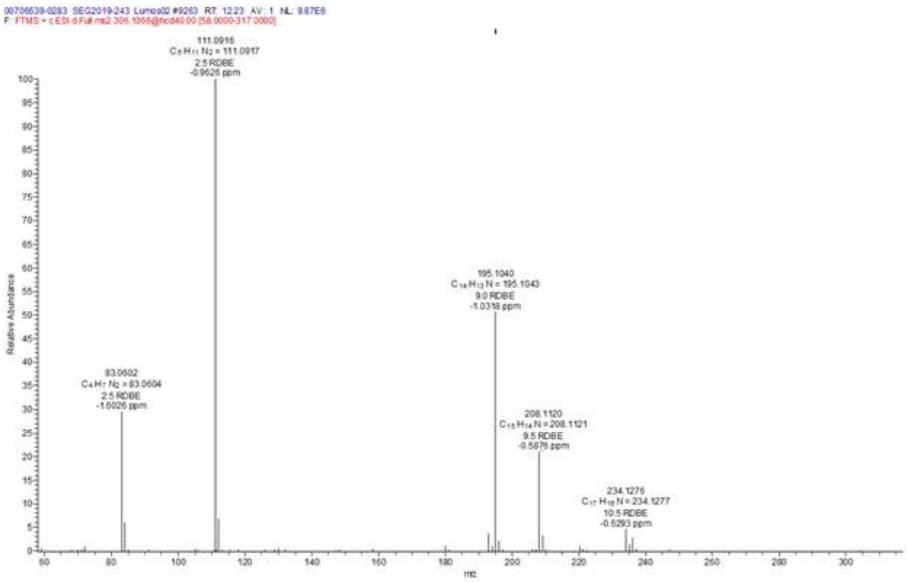

Figure S13: Mass Spectrum for **p4**

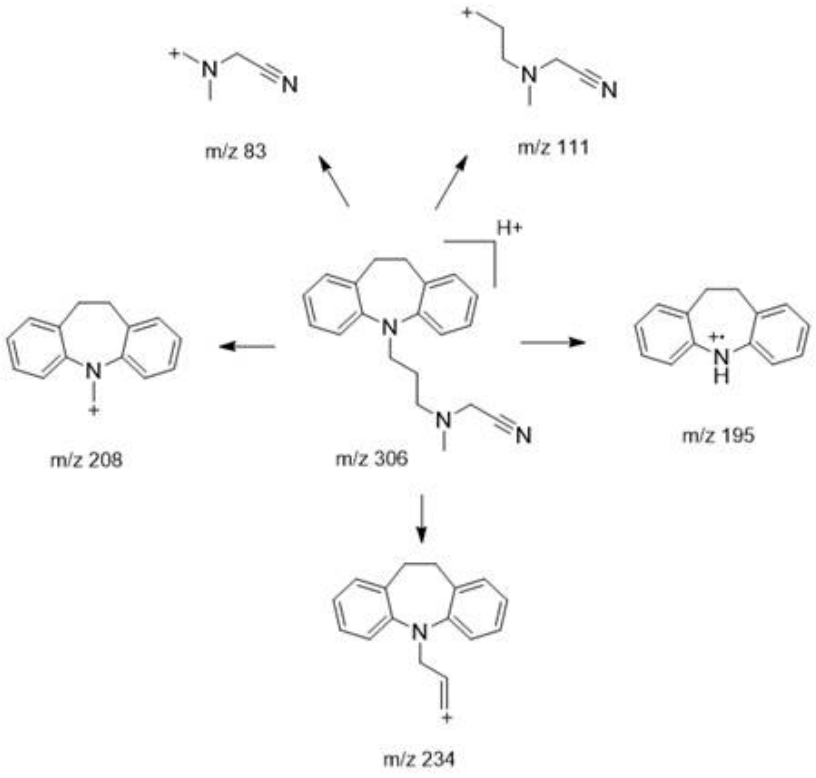

Figure S14: MS fragmentation pattern for **p4**

Mass Spectrometry Results for N-oxide (p5)

High resolution accurate mass measurements of N-oxide (**p5**) showed the molecular ion [M+H]+ at *m/z* value of 297.1961 that correlates to a protonated empirical formula of $C_{19}H_{25}N_2O+$ with a deviation of -0.2 ppm from the theoretical mass. The MS^2 of *m/z* 297 gave major fragment ions at *m/z* 102 resulting from the loss of the iminodibenzyl (**p2**) moiety and *m/z* 195 resulting from the loss of N,N-dimethylpropan-1-amine oxide. The MS^2 of *m/z* 297 yielded additional fragment ions *m/z* 208 (loss of N,N-dimethylethanamine oxide), *m/z* 236 (loss of C_2H_6NO), *m/z* 72 (loss of 5-(methyl) iminodibenyzl (**p2**) plus oxygen), and *m/z* 84 (loss of iminodibenzyl (**p2**) plus oxygen).

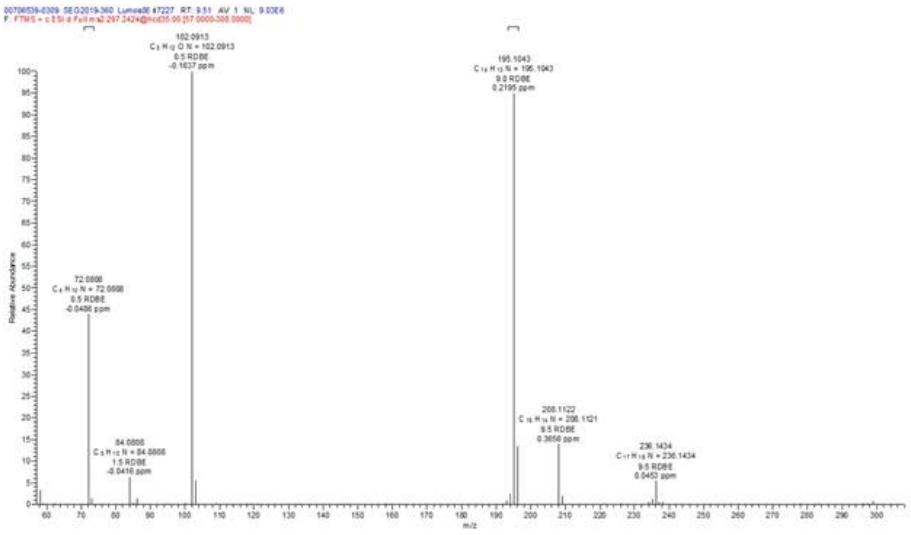

Figure S15: Mass Spectrum of N-oxide **(p5)**

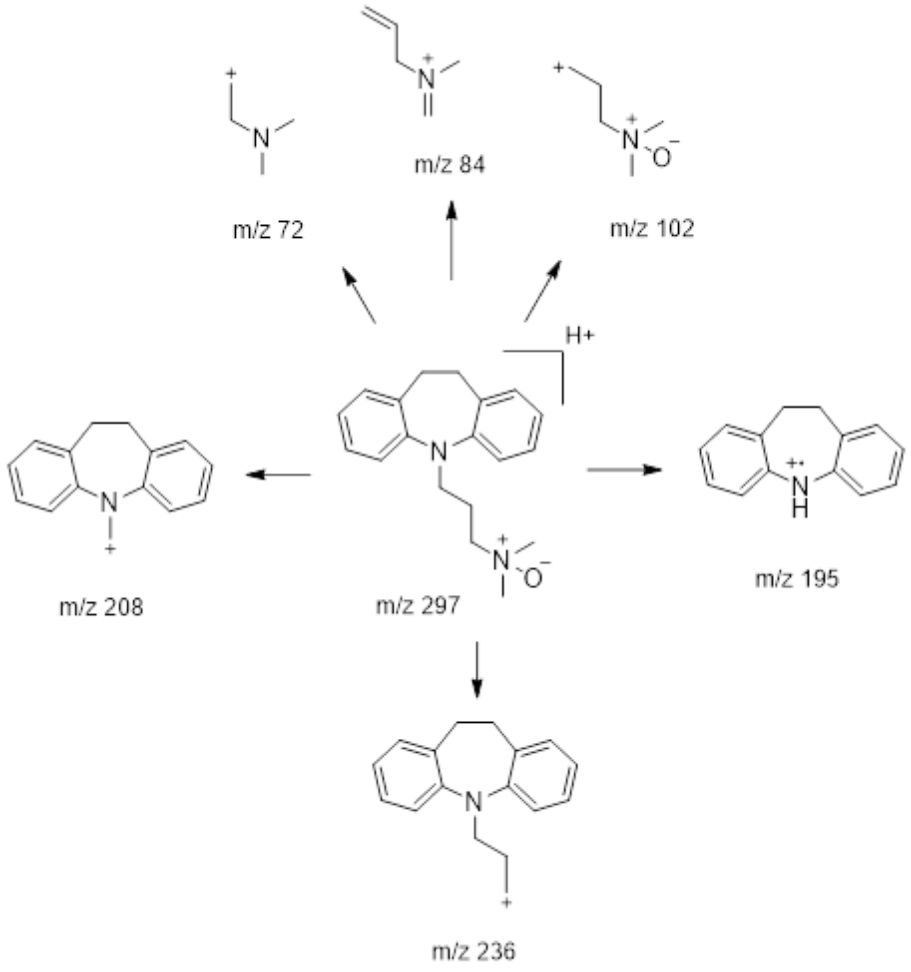

Figure S16: MS fragmentation pattern of the N-oxide **(p5)**

Nuclear Magnetic Resonance Experimental for N-oxide (p5)

All 1D and 2D data were collected at 298 K using a Bruker BioSpin 5mm TCI cryoprobe on an AVANCE III NMR spectrometer (Bruker-BioSpin, Billerica, Massachusetts) operating at 600 MHz. The following data were collected: 1D proton, 1D carbon, ^{1}H-^{1}H gradient COSY (Correlation Spectroscopy), ^{1}H-^{13}C multiplicity edited HSQC (Heteronuclear Single Quantum Coherence), and ^{1}H-^{1}H Tr- ROESY (Transverse Rotating-frame Overhauser Effect Spectroscopy). A ∼3 mg sample of N-oxide (**p5**) was dissolved in 0.2 mL of 99.96% deuterated dimethylsulfoxide (DMSO-d_6) with 0.05% V/V tetramethylsilane (TMS). A ∼10 mg sample of imipramine HCl was also dissolved in 0.2 mL of 99.96% deuterated dimethylsulfoxide (DMSO-d_6) with 0.05% V/V tetramethylsilane (TMS). The 1D proton and carbon spectra were referenced using TMS signal and the central peak of the DMSO-d_6 ^{13}C multiplet signals, set to 0.00 ppm and 39.51 ppm, respectively. 1D and extensive 2D NMR experiments were performed for the assignments of the proton and carbon spectra for an N-oxide (**p5**) (Figures S17 and S18) and imipramine (Figures S19 and S20). The data are consistent with structures N-oxide (**p5**) and imipramine. Figure S21 shows the proton and carbon chemical shift assignments for each compound. The site of N-oxidation can be determined by carbon chemical shift perturbation. Significant carbon chemical shift changes between N-oxide (**p5**) and imipramine due to an electron-withdraw oxygen occurred at both carbons of N-dimethyl group and a carbon alpha to N-dimethyl group. Both carbons of N-dimethyl group and a carbon alpha to N-dimethyl group of an N-oxide (**p5**) experience of $\sim$ 17 ppm deshielded and $\sim$ 14ppm deshielded, respectively as compared to those of imipramine, indicating that the site of N-oxidation occurred at the nitrogen of N-dimethyl group. Our NMR data (in DMSO-d_6) are consistent with previously published by Gowda, N. B., Rao, G. K., and Ramakrishna R. A. *Tetrahedral Lett.* **2010**, *51*, 5690-5693.

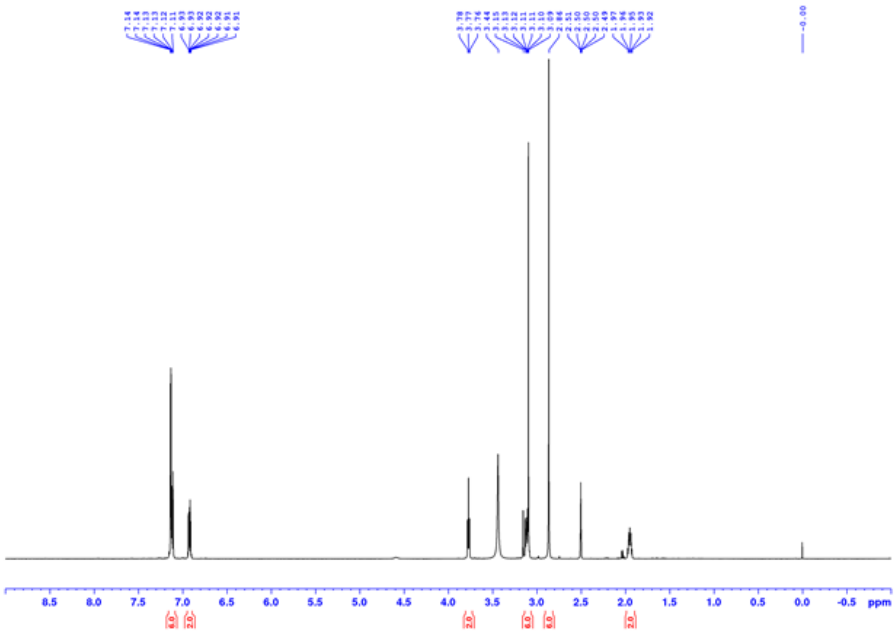

Figure S17: ^{1}H NMR Spectrum of N-oxide **(p5)**

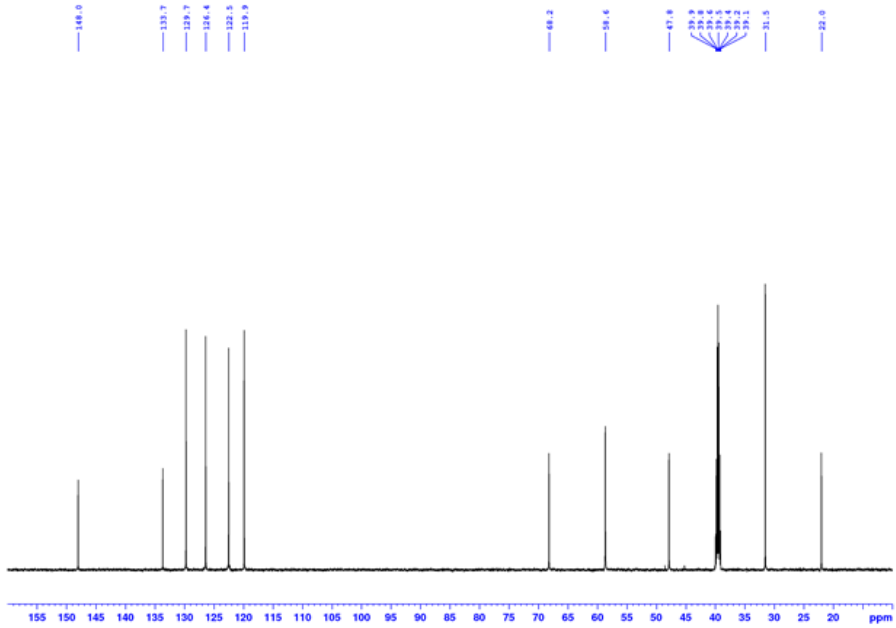

Figure S18: ^{13}C NMR Spectrum of N-oxide **(p5)**

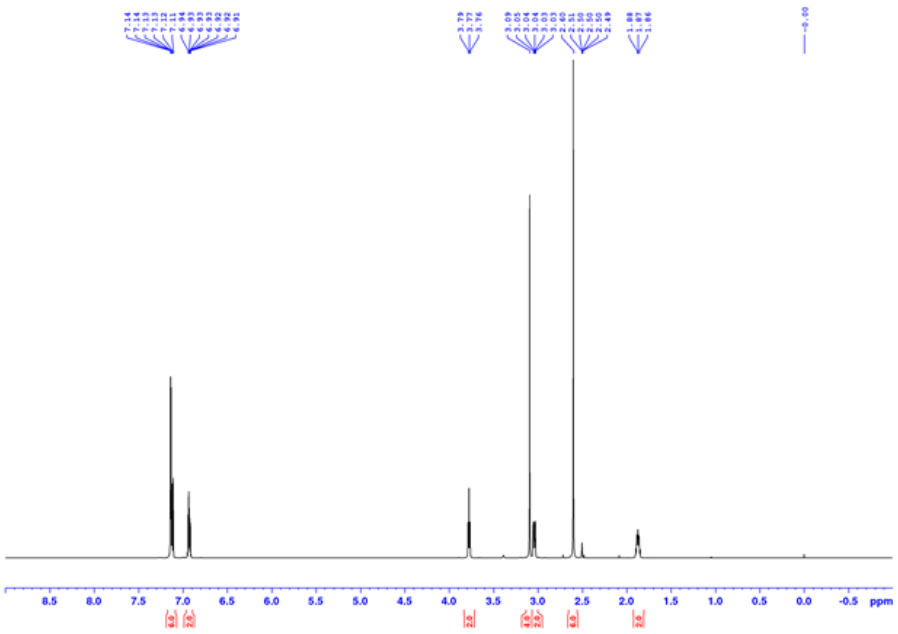

Figure S19: ^{1}H NMR Spectrum of Imipramine

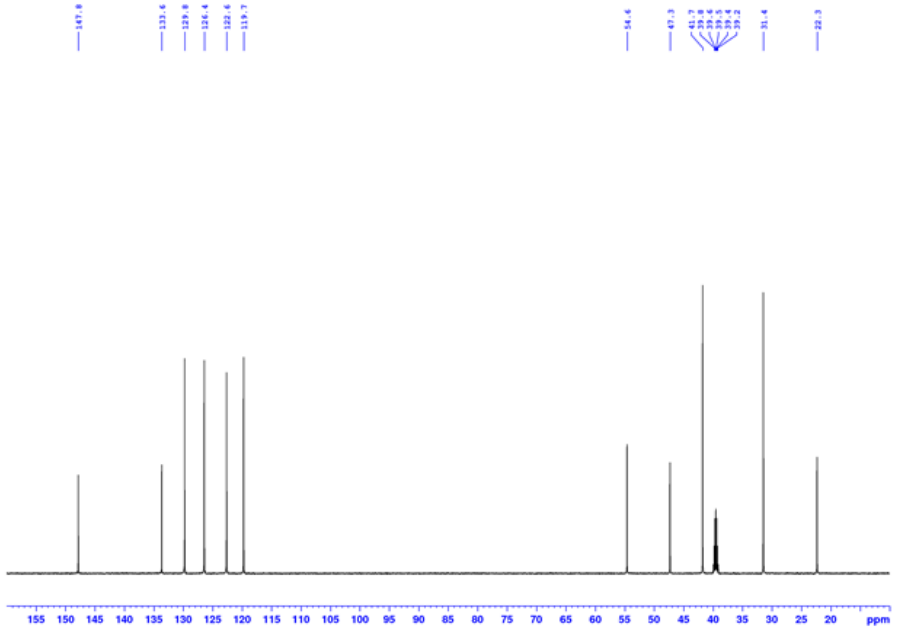

Figure S20: ^{13}C NMR Spectrum of Imipramine

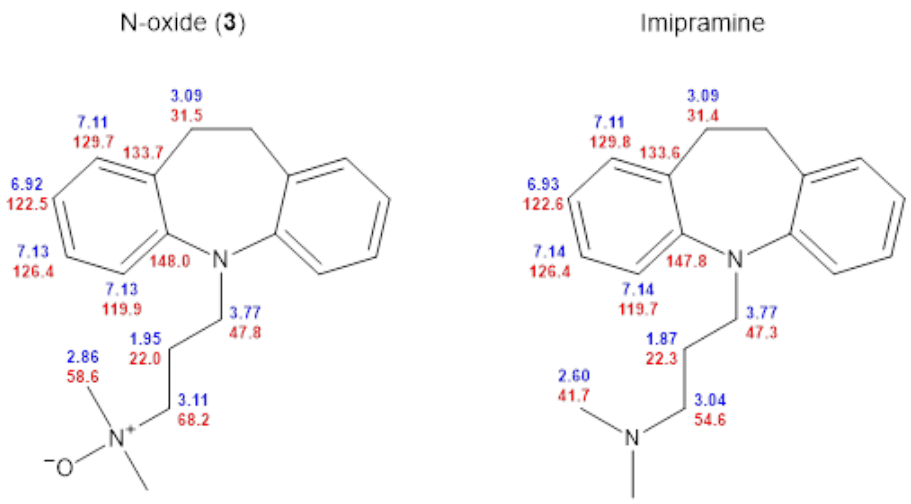

Figure S21: ^{1}H (blue) and ^{13}C NMR (red) chemical shift assignments for N-oxide **(p5)** and Imipramine

References

[1] J.-D. Chai, M. Head-Gordon, Long-range corrected hybrid density functionals with damped atom-atom dispersion corrections, Physical Chemistry Chemical Physics 10 (44) (2008) 6615–6620. doi:10.1039/b810189b.

[2] L. Goerigk, A. Hansen, C. A. Bauer, S. Ehrlich, A. Najibi, S. Grimme, A look at the density functional theory zoo with the Advanced GMTKN55 database for general main group thermochemistry, Kinetics and noncovalent interactions, Physical Chemistry Chemical Physicsdoi:10.1039/C7CP04913G.

[3] C. Riplinger, F. Neese, An efficient and near linear scaling pair natural orbital based local coupled cluster method, The Journal of Chemical Physics 138 (3) (2013) 034106. doi:10.1063/1.4773581.

[4] D. G. Liakos, M. Sparta, M. K. Kesharwani, J. M. L. Martin, F. Neese, Exploring the Accuracy Limits of Local Pair Natural Orbital Coupled-Cluster Theory, Journal of Chemical Theory and Computation 11 (4) (2015) 1525–1539. doi:10.1021/ct501129s.

[5] D. G. Liakos, F. Neese, Is It Possible to Obtain Coupled Cluster Quality Energies at near Density Functional Theory Cost? Domain-Based Local Pair Natural Orbital Coupled Cluster vs Modern Density Functional Theory, Journal of Chemical Theory and Computation 11 (9) (2015) 4054–4063. doi:10.1021/acs.jctc.5b00359.

[6] C. Riplinger, P. Pinski, U. Becker, E. F. Valeev, F. Neese, Sparse maps–A systematic infrastructure for reduced-scaling electronic structure methods. II. Linear scaling domain based pair natural orbital coupled cluster theory, Journal of Chemical Physics 144 (2) (2016) 024109. doi:10.1063/1.4939030.

[7] D. G. Liakos, Y. Guo, F. Neese, Comprehensive Benchmark Results for the Domain Based Local Pair Natural Orbital Coupled Cluster Method (DLPNO-CCSD(T)) for Closed- and Open-Shell Systems, The Journal of Physical Chemistry A 124 (1) (2020) 90–100. doi:10.1021/acs.jpca.9b05734.

[8] E. Semidalas, J. M. L. Martin, Canonical and DLPNO-Based G4(MP2)XK-Inspired Composite Wave Function Methods Parametrized against Large and Chemically Diverse Training Sets: Are They More Accurate and/or Robust than Double-Hybrid DFT?, Journal of Chemical Theory and Computation 16 (7) (2020) 4238–4255. doi:10.1021/acs.jctc.0c00189.